# Combustion synthesis/quasi-isostatic pressing of TiC–NiTi cermets: processing and mechanical response

E. R. Strutt · E. A. Olevsky · M. A. Meyers

**Abstract** TiC–NiTi composites were produced by a technique combining self-propagating high-temperature synthesis (SHS) of elemental powders of Ni, Ti, and C with densification by quasi-isostatic pressing (QIP). In order to create a one-step synthesis/densification process, the Ti + Ni + C reactant material was surrounded in a bed of graphite and alumina particulate before initiation of the combustion reaction. The sample was ignited within the particulate and subjected to a uniaxial load immediately after passage of the combustion wave. The constitutive response, composition and resulting structures of the composites with varying volume fractions of NiTi are characterized. Powder mixtures prepared anticipating the formation of stoichiometric TiC result in the formation of composites with a eutectic matrix of $Ni_3Ti$ and NiTi. This titanium impoverishment of the matrix is consistent with the formation of nonstoichiometric $TiC_x$ during the combustion reaction. The $Ni_3Ti$ phase can be suppressed by anticipating the formation of $TiC_{0.7}$ and adjusting the chemical content of the reactant mixture to include additional titanium. These cermets combine the high hardness of the ceramic phase with the possible shape memory and superelastic effects of NiTi.

E. R. Strutt · M. A. Meyers
Materials Science and Engineering Program, University of California, San Diego, La Jolla, CA 92093-0411, USA

E. A. Olevsky
Department of Mechanical Engineering, San Diego State University, San Diego, CA 92182-1323, USA

M. A. Meyers (✉)
Departments of Mechanical and Aerospace Engineering and Nanoengineering, University of California, San Diego, La Jolla, CA 92093-0411, USA
e-mail: mameyers@ucsd.edu

## Introduction and objectives

In 1977, Goldstein was issued a patent for the synthesis of TiC–NiTi armor plate by infiltration of porous carbon with a Ti-rich Ni–Ti alloy, followed by heating to provide solid-state conversion of the carbon into TiC [1]. Goldstein used NiTi as the matrix for his composites, because of its shape memory and super-elastic effects. He recognized that these additional mechanisms of strain accommodation could act to toughen ceramic-based composites and provide a damage-tolerant armor material with potential multiple-hit capability. Dunand and coworkers continued this effort and produced NiTi–TiC by mixing of powders and hot pressing [2–5]. They systematically investigated the microstructure and mechanical properties.

Combustion synthesis is a well-established technique for the production of ceramics especially in combination with densification, such as high-speed forging [6, 7] and quasi-isostatic pressing [8, 9], using a granular pressure-transmitting medium. Self-propagating high-temperature synthesis (SHS) uses the energy of the exothermic reaction between elemental metal and nonmetal powders to sustain the reaction as a combustion wave [10–12]. This process results in the complete conversion from reactants to products within seconds after ignition.

The overall goal of this research was to produce the $TiC_x$–NiTi composites with varying volume fractions of NiTi by SHS. The first objective of this research was to investigate the effectiveness of the densification technique known as quasi-isostatic pressing (QIP) in the removal of porosity from the as-synthesized material. Fully dense ceramics had been produced earlier by our group but this required the use of a dynamic forging machine (Dynapak) [6, 7, 13–16]. QIP is an inexpensive technique that uses granular particulate to provide lateral confinement to powder and porous materials

during uniaxial loading. Optimization of densification parameters (configuration, load, delay time) depended largely on "trial and error." In an attempt to reduce the empirical nature of the process, the theory on densification of nonlinear-viscous porous materials developed by Skorohod and Olevsky [17–19] was combined with indentation experiments to determine the constitutive response of the material in earlier work [20, 21]. We use two simpler constitutive equations in the present contribution.

## Materials

Since $TiC_x$ exists over a wide range of compositions, and NiTi has a very narrow range of stability, synthesis of $TiC_x$–NiTi composites from elemental Ti, Ni, and C powders requires careful tailoring of the reactant chemistry. The starting materials used in this investigation were high-purity powders of Ti, C, and Ni. The average particle sizes for Ti, C, and Ni were 44, 2, and 3 μm, respectively. The following basic reactions were studied:

$$(1 + y)Ti + C + yNi \rightarrow TiC + yNiTi$$

$$(1 + z)Ti + 0.7C + zNi \rightarrow TiC_{0.7} + zNiTi$$
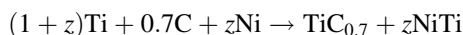
Powders were mixed in order to obtain product compositions corresponding to volume fractions of NiTi between 0.1 and 0.8. Since the actual quantities of powder were measured by weight and not volume, the volume fractions were converted to mole fractions according to the following formulae:

$$x_{Ni} = \left(\frac{a_{TiC_x}}{a_{NiTi}}\right)\left(\frac{\rho_{NiTi}}{\rho_{TiC_x}}\right)\left(\frac{v_{NiTi}}{1 - v_{NiTi}}\right)\left(\frac{x_C}{x}\right)$$

$$x_{Ti} = \frac{x_C}{x} + x_{Ni}$$

where $a$ is the molecular weight, $\rho$ is the density, $v$ is the volume fraction, $x_{Ni}$, $x_{Ti}$, and $x_C$ are the mole fractions of Ni, Ti and C, respectively, and $x$ is the stoichiometric coefficient of the carbide (either 1 or 0.7 in these experiments). Table 1 lists the molecular weights and densities for the carbide and NiTi.

The value of $\rho_{TiC_{0.7}}$ had to be calculated because vacancies on the carbon sublattice of the titanium carbide B1 structure reduce the mass of the unit cell and the change its volume. When there are no vacancies on the carbon

**Table 1** The molecular weights and densities of TiC, $TiC_{0.7}$, and NiTi

|  | TiC | $TiC_{0.7}$ | NiTi |
| --- | --- | --- | --- |
| $a$ (g/mol) | 59.89 | 56.31 | 106.57 |
| $\rho$ (g/cm³) | 4.93 | 4.62 | 6.45 |

**Table 2** Weight of Ti, C, and Ni in a 100 g mixture of powder

| Expected product composition | Weight of Ti powder (g) | Weight of C powder (g) | Weight of Ni powder (g) |
| --- | --- | --- | --- |
| TiC–10NiTi | 75.5 | 17.5 | 7.0 |
| TiC–20NiTi | 71.3 | 15.1 | 13.6 |
| TiC–30NiTi | 67.4 | 12.8 | 19.8 |
| TiC–40NiTi | 63.6 | 10.7 | 25.7 |
| TiC–50NiTi | 60.1 | 8.7 | 31.2 |
| $TiC_{0.7}$–10NiTi | 77.3 | 12.1 | 10.6 |
| $TiC_{0.7}$–20NiTi | 74.6 | 11.0 | 14.4 |
| $TiC_{0.7}$–30NiTi | 70.1 | 9.3 | 20.6 |
| $TiC_{0.7}$–40NiTi | 65.6 | 7.7 | 26.7 |
| $TiC_{0.7}$–50NiTi | 61.7 | 6.2 | 32.1 |
| $TiC_{0.7}$–60NiTi | 57.9 | 4.8 | 37.3 |
| $TiC_{0.7}$–70NiTi | 54.3 | 3.5 | 42.2 |
| $TiC_{0.7}$–80NiTi | 51.0 | 2.3 | 46.7 |

sublattice, the space lattice of titanium carbide is fcc with a basis of one Ti atom at 000 and one C atom at 1/2, 1/2, 1/2. There are four Ti atoms and four C atoms per unit cell. In $TiC_{0.7}$, vacancies on the carbon sublattice reduce the number of carbon atoms in the unit cell to 2.8 (4 multiplied by the stoichiometric coefficient 0.7). This lower number of atoms obviously reduces the total mass of the unit cell to $37.4 \times 10^{-23}$ g as compared to $39.8 \times 10^{-23}$ g for the stoichiometric carbide. In addition, the lattice parameter of the titanium carbide unit cell changes with the Ti/C atom ratio. $TiC_{0.7}$ has a lattice parameter of approximately 0.4326 nm [22], which results in a unit cell volume of $8.1 \times 10^{-20}$ mm³. Dividing the mass of the unit cell by its volume gives a calculated density for $TiC_{0.7}$ of $4.62 \times 10^3$ kg/m³.

Once the desired mole fractions of Ti, C, and Ni were determined, they were multiplied by their respective atomic weights. Table 2 lists the weights of each component in a 100 g mixture of powder.

## Experimental procedures

### Cold pressing

The powders were loaded under argon into polyethylene jars and dry mixed with burundum™ grinding medium (4:1 by weight) for 24 h. They were then baked in a vacuum oven for a minimum of 16 h at approximately 100 °C and a pressure less than 100 mmHg in order to remove adsorbed water. After baking, the powders were uniaxially pressed into either 25 g compacts with a diameter of 30 mm and height of 10 mm or 300 g compacts with a diameter of 76 mm and height of approximately 25 mm. The goal was

to apply enough pressure so that the compacts could be handled without falling apart, but not so much that circumferential cracking would occur. In order to create 300 g cylindrical compacts with a diameter of 76 mm, an applied pressure of 20 MPa was sufficient.

Mechanical testing

Quasi-static compression tests were performed above and below the $R_s$ temperature in order to determine if stress-induced transformation or variant reorientation could be detected. Tests were performed using an Instron machine specially equipped with a Research Incorporated radiant furnace and ceramic compression arbor. The radiant furnace was composed of four 500 W tungsten light bulbs set in a quad elliptical mirrored chamber. Each lamp was positioned at one foci of one of the elliptical sub-chambers. The sample was positioned so that it sat at the other foci, which was common for each of the four elliptical sub-chambers. A controller was used to monitor the output of a thermocouple in the chamber, compare this temperature to a set value, and adjust the voltage to the lamps accordingly. A thermocouple was also placed directly in contact with the sample.

The $TiC_{0.7}$–30NiTi composites for the quasi-static compression tests were cut by electrodischarge machining into cylindrical samples, 3.8 mm in diameter and 6 mm in height. Strain gages were attached to the samples in order to study the mechanical behavior at strains less than 1%. During quasi-static compression testing, the $TiC_{0.7}$–30NiTi samples were sandwiched between silicon nitride whisker reinforced silicon carbide platens.

The constitutive response of the $TiC_{0.7}$–30NiTi composite was established by performing indentation experiments [20, 21]. A disk-shaped green compact was placed in a uni-axial testing machine (Instron) and ignited. After the reaction was complete, a cylindrical indenter was moved onto the specimen at a prescribed velocity, producing an indentation. The velocity of the sintered SiC indenter was 0.4 m/s. The resulting stress–strain curve was recorded and the data were used along with the theory of densification of nonlinear-viscous porous materials to calculate the constitutive parameters.

Combustion synthesis and densification procedure

The experimental configuration for the synthesis and densification of the 30 mm samples is shown in Fig. 1a. The experimental configuration for the synthesis and densification of the compacts with a diameter of 76 mm is shown in Fig. 1b. The fixture used to contain the 76 mm samples was designed by La Salvia and Meyers [14] and consisted of a steel cup insulated with two layers of $Al_2O_3$–$SiO_2$
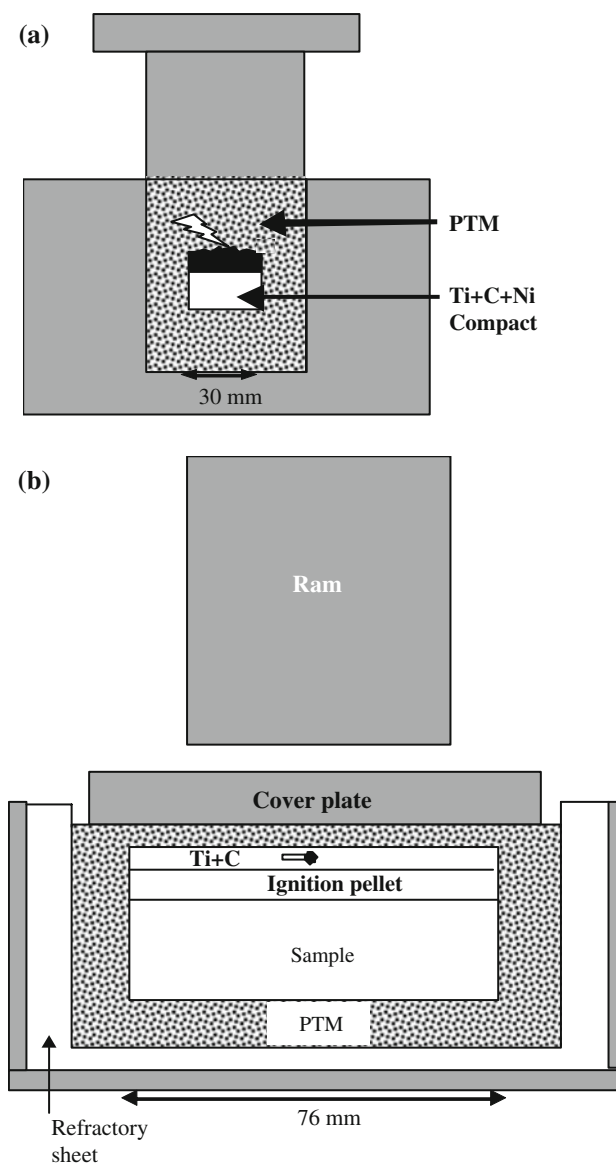


Fig. 1 Containment fixture for samples with (a) 3 cm diameter and (b) 7.6 cm diameter

refractory sheet (Zircar RSDR-3 mm thick). For thermal insulation and to redistribute the applied axial load, the sample was surrounded by an alumina/graphite granular medium. Figure 2a shows a backscattered electron micrograph of this granular pressure-transmitting medium (PTM). The particles were originally within 60–300 μm (230–50 mesh). The alumina particles were tabular-shaped with closed intergranular pores. The graphite particles were generally spheroidal in shape with outward projecting nodules and surface fissures (see arrows). After repeated use the particles break-up into fragments as shown in Fig. 2b. The use of PTM was pioneered by Merzhanov and co-workers [23], and was later implemented in the SHS by Raman et al. [24] who successfully produced plates with dimensions of 250 × 250 × 25 mm.
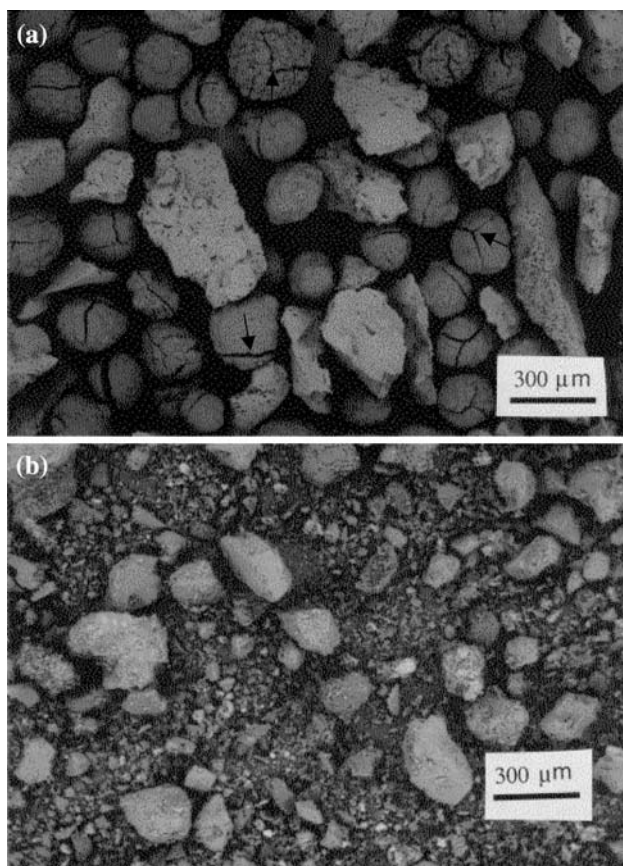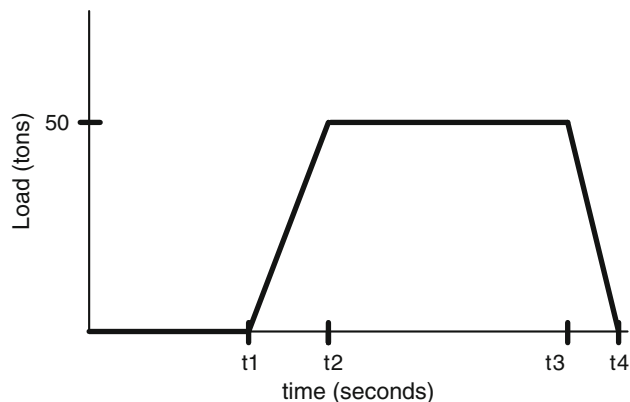
Fig. 2 Backscattered electron micrograph of alumina/graphite granular pressure transmitting medium: (**a**) before pressing and (**b**) after many SHS/QIP cycles



Fig. 3 Schematic representation of the loading as a function of time during the QIP densification process

To aid the initiation of a planar combustion wave, the sample was placed beneath a grafoil disk and a layer of loose Ti + C reactant powder. In some cases, a compact of pressed Ti + C powder was also used, shown in Fig. 1b and labeled ignition pellet. An electrochemical match consisting of Ni–Cr wire wrapped around a wooden matchstick was buried in the loose powder and ignited. Ignition was marked by the ejection of granular media from the containment fixture.

Ignition of the combustion reaction was consistently successful when the ignitors were made from "DURA-FLAME" long stem safety matches. Smaller matches did not provide enough heat input to initiate the self-propagating reaction. Successful ignition also required that there be no preload on the sample and no contact between the ignition wires and the metal die.

After ignition and reaction, the samples were mechanically loaded to remove residual porosity. Figure 3 shows a schematic representation of the loading as a function of time. The time $t_1$ (often referred to as the delay time) represents the time between ignition and the beginning of consolidation. In the present study, $t_1$ was between 5 and

30 s. The difference between $t_2$ and $t_1$ ($t_2 - t_1$) is the time to maximum load. In these experiments the samples were loaded by an Enerpac H frame 100 ton capacity press to a maximum load between 50 and 70 tons. The time to reach the maximum load was approximately 10 s. The time ($t_3 - t_2$) is the holding time under load and was set at 10 s. The unloading time ($t_4 - t_3$) was about 1 s. After densification the samples were placed in vermiculite for slow cooling. The characteristic times during the QIP densification sequence are given in Table 3.

Figure 4a, b shows the effectiveness of the QIP densification sequence for removing the porosity in SHS products. The large voids and lateral channels created during the SHS process are shown in Fig. 4a for a TiC–40vol%NiTi composite. In Fig. 4b, these voids have been collapsed by applying a 125 MPa pressure after a delay time of 10 s. The optimum delay time and pressure were dependent on sample composition and size. For the 76-mm diameter samples, the delay times and loads had to be adjusted to ensure pore collapse while avoiding material extrusion from the containment cup. Surprisingly, the samples with 80 vol% NiTi were the most difficult to consolidate. Molten material was ejected from the containment cup immediately after contact with the densification punch. This underscores the importance of adjusting the delay time and the gap between the punch and containment cup rim.

All values quoted in this article refer to volume fractions.

**Table 3** Characteristic times during QIP densification of SHS produced TiC$_x$–NiTi composites

| Parameter | | Time (s) |
|---|---|---|
| Delay time | $t_1$ | 10–30 |
| Loading time | $t_2 - t_1$ | 10–15 |
| Holding time | $(t_3 - t_2)$ | 10 |
| Unloading time | $(t_4 - t_3)$ | 1–2 |

**Fig. 4** TiC–40vol%NiTi, (**a**) as-reacted material, not subject to post-reaction densification, (**b**) reacted and densified
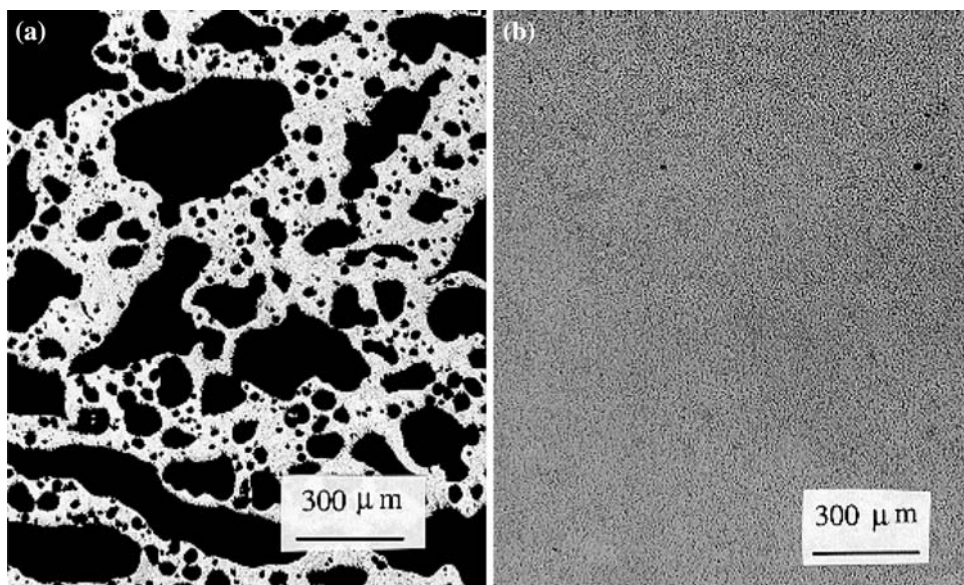


## Resulting microstructures and mechanical properties

### Constitutive response

Figure 5 shows the cross-section of the indented $TiC_{0.7}$–30NiTi specimen. In order to obtain an analytical solution of the indentation process, the uniaxial upsetting of a porous cylinder with a radius smaller than the indenter was modeled. Friction was neglected, as well as the distortion of the compact outside of the main deformation zone.

In previous research, the Skorohod–Olevsky constitutive equation was used. Whereas Skorohod and Olevsky [17, 18] and Olevsky et al. [20, 21] described the densification process of nonlinear-viscous porous materials based on a rheological constitutive relationship connecting components of stress tensor $\sigma_{ij}$ and strain rate tensor $\dot{e}_{ij}$, in the current work two simpler models are used. They are briefly described below.

The Fischmeister–Arzt constitutive model [25] is based on the plastic deformation of spheres with equal radius $R$. The area of contact gradually increases from $A_0 = 0$ to $A$. The coordination number for each sphere, $Z$, produces the number of contact areas.

The compressive stress required to make an indentation on a surface is equal to $\sim 3\sigma_0$, where $\sigma_0$ is the yield stress of the material. It can be shown that [25]:

$$3\sigma_0 = \frac{4\pi R^2}{AZD} P \qquad (1)$$

where $D$ is the relative density. Helle et al. [26] assumed that $Z = 12D$.

As densification takes place, the contact area, $A$, between particles increases due to flattening. This contact area (for particles) is expressed as

$$A = \frac{4\pi R^2 D}{Z}\left(\frac{D - D_0}{1 - D_0}\right) \qquad (2)$$

**Fig. 5** Cross-section of indented $TiC_{0.7}$–30NiTi specimen that shows the material distortion during loading. Full densification occurs under the indenter



Indenter
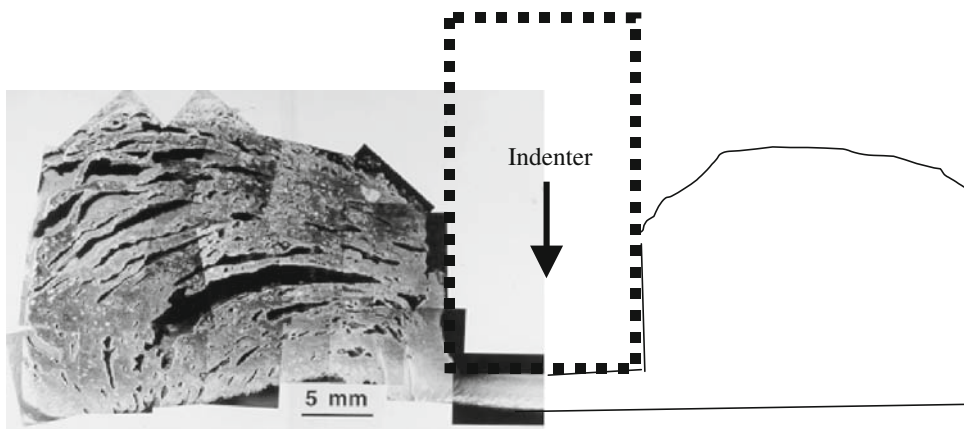
For full densification, it is equal to the surface of the sphere, $4\pi R^2$.

Substituting Eq. 1 into 2

$$P = 3\sigma_0 \frac{D^2(D - D_0)}{(1 - D_0)} \tag{3}$$

Equation 3 gives a relationship between the pressure and the relative density. It is plotted in Fig. 7a from an initial relative density of 0.15 and different values of the flow stress $\sigma_0$. The Torre–Carroll–Holt equation [27, 28] is obtained by the application of an analytical treatment to the configuration shown in Fig. 6b. The hollow sphere can be used to define a relative density

$$D = \frac{b^3 - a^3}{b^3} \tag{4}$$

where $b$ is the outer radius and $a$ is the inner radius.

In spherical coordinates, the equilibrium equation of stresses acting on an element (shown in Fig. 6b) is:

$$\frac{d\sigma_r}{dr} + \frac{2}{r}(\sigma_r - \sigma_\theta) = 0 \tag{5}$$

where $\sigma_r$ and $\sigma_\theta$ are the radial and circumferential stress components, and $r$ is the radius.

The boundary conditions are:

$\sigma_r = -P \quad \text{at } r = b$

$\sigma_r = 0 \quad \text{at } r = a$

We assume that Tresca's criterion holds, i.e., plastic flow occurs when

**(a)**

**(b)**
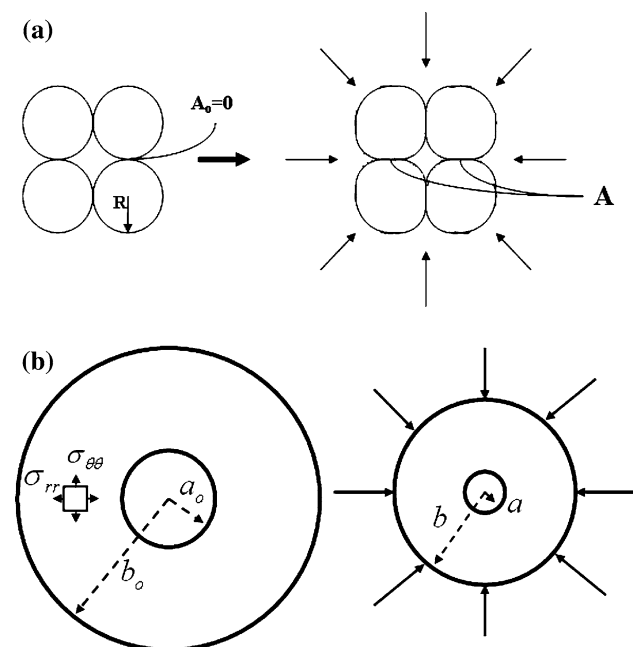
Fig. 6 Two physically based densification mechanisms: (a) particle flattening (Fischmeister–Arzt) densification mechanism and (b) hollow sphere model (Torre–Carroll–Holt)

$$\sigma_r - \sigma_\theta = \sigma_0 \tag{6}$$

where $\sigma_0$ is the flow stress. By substituting Eq. 6 into Eq. 5 and integrating it from $a$ to $b$, we have:

$$\int_a^b d\sigma_r = -2\sigma_0 \int_a^b \frac{dr}{r} \tag{7}$$

$$\sigma_r \vert_a^b = -P = -2\sigma_0 \ln \frac{b}{a} = -\frac{2}{3}\sigma_0 \ln \frac{b^3}{a^3} \tag{8}$$

Substituting Eq. 4:

$$\text{Hence} \quad P = \frac{2}{3}\sigma_0 \ln \frac{1}{1 - D} \tag{9}$$

This equation is plotted in Fig. 7b for the same value of $\sigma_0$ as the FA equation in Fig. 7a. The initial porosity seen in Fig. 4a can be divided into two types: larger pores with $\sim 300$ μm diameter and smaller spheroidal pores with $\sim 10$–$50$ μm. In physical terms, the FA equation decreases the flattening of the large voids, whereas the TCH equation represents the collapse of the small voids. Compared with FA particle flattening model, the TCH pore collapse model predicts much higher pressures to achieve full densification ($P/\sigma_0 > 5$). In this context, it is more realistic for higher relative densities ($D > 0.9$). It should be noted that when powders are pressed in cylinders, additional frictional effects at the walls have to be considered. Another complication is that the state of stress deviates from hydrostatic. The experimental densification curve is compared with the two constitutive equations in Fig. 7c. One may conclude the early response is best described by the FA constitutive equation (with $\sigma_0 = 10$ MPa), whereas the final densification is best described by the TCH equation (with $\sigma_0 = 30$ MPa). This response is consistent with the two mechanisms of void closure: flattening of larger voids (FA) followed by the hydrostatic collapse of the smaller voids (TCH). It is apparent that the densification is not an isothermal process and that the specimen cools during densification. This is shown by the increase in flow stress from 10 to 30 MPa.

Product composition

*TiC–NiTi composites*

Figure 8a shows the backscattered electron micrograph of the TiC–40NiTi composite. The matrix appears to be composed of two phases. X-ray diffraction was used to determine the individual phases present within the composite. The scan was performed using CuKα radiation with a Scintag XRD-2000 Theta-Theta diffractometer. The $2\theta$ angles considered were between 35° and 80°, with a step increment of 0.1°. The X-ray diffraction scan of the TiC–30NiTi composite is shown in Fig. 8b. Comparison of the
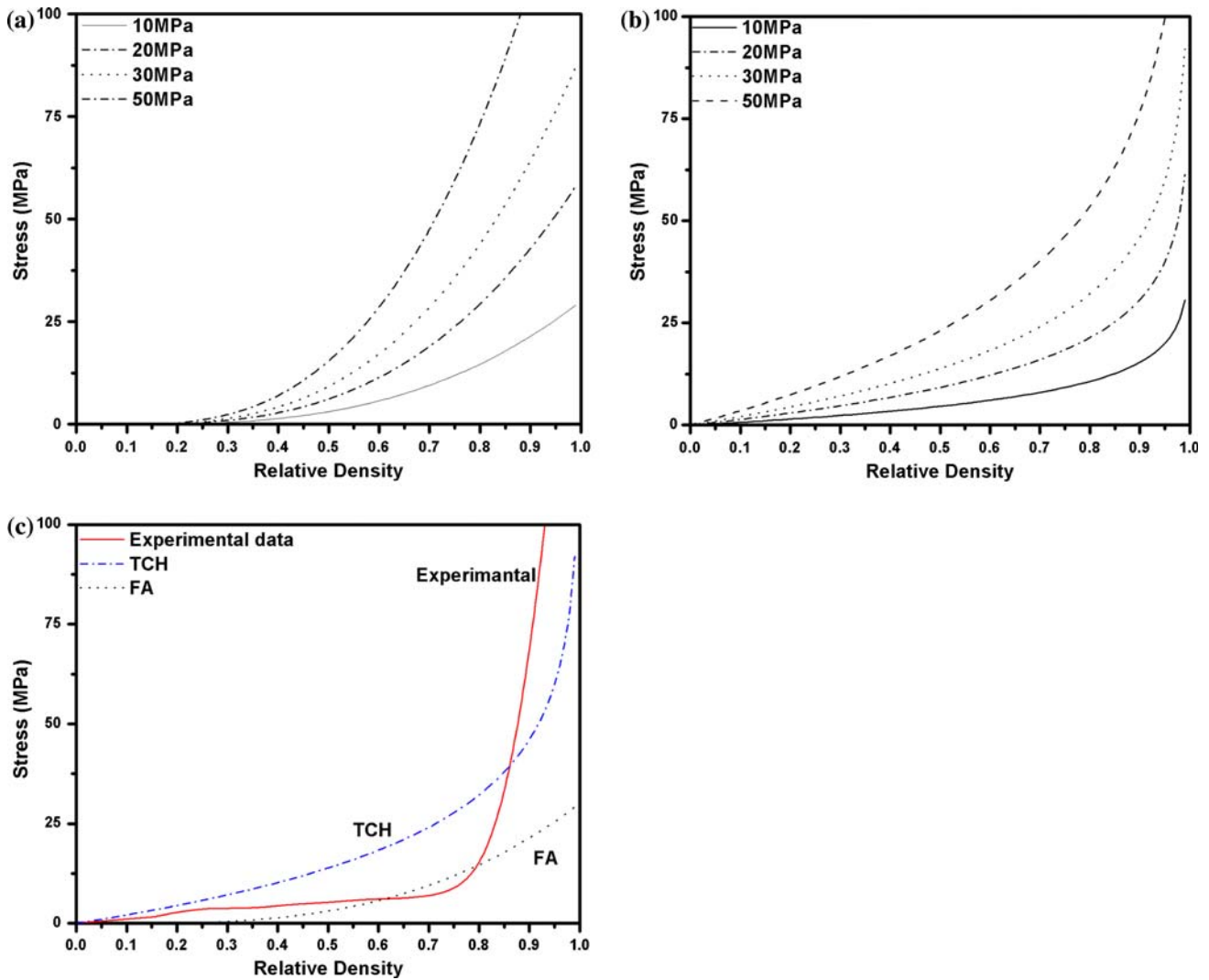
**Fig. 7** Implementation of (**a**) Fischmeister–Artz and (**b**) Torre–Carroll–Holt constitutive models of different yield stresses $\sigma_0 = 10, 20, 30$, and 50 MPa; (**c**) experimentally obtained stress densification response of SHS product ($TiC_{0.7}$–30NiTi) and comparison with FA and TCH models

peak locations in the scan with those listed in the JCPDS Powder Diffraction file confirmed the presence of TiC, NiTi, and $Ni_3Ti$. Although $Ni_3Ti$ was not anticipated as a product phase, it was repeatedly the dominant matrix phase in samples where stoichiometric titanium carbide was expected.

In order to determine if titanium was boiling off during the SHS reaction, the adiabatic temperatures for the TiC–NiTi system were calculated. These calculations, although neglecting heat losses to the environment, provided an upper bound to sample temperature. The results are shown in Fig. 9. The maximum possible temperatures achieved during the reactions were always lower than the boiling point of titanium (3357 °C) and nickel (2911 °C). Ti has a much higher vapor pressure than Ni and this could account for some loss in the liquid state ($M_p = 1660$ °C). We do not have direct evidence for this. Another possibility for

the loss of titanium from the matrix is the formation of nonstoichiometric carbide.

The Ti–C binary phase diagram [29] indicates that $TiC_x$ exists as a single phase over a range that extends from $x = 0.49$ to 1.0. Such a wide compositional range is caused by vacancies on the carbon sublattice of the B1 structure (sodium chloride). If nonstoichiometric $TiC_x$ forms during the SHS production of TiC–NiTi composites, there will be a loss of Ti from the matrix. Redistribution of Ti atoms from the matrix to the carbide has been observed during the sintering of near stoichiometric micron-sized TiC and NiTi powders (sintered 1 h at 1300 °C) [30, 31]. It was shown that when the weight percentage of NiTi varies between 40 and 70 (34–64 vol% NiTi), the sintering process was accompanied by recrystallization through a solution-precipitation mechanism and the lattice parameter of the $TiC_x$ decreased. The lattice parameter of $TiC_x$ varied as a
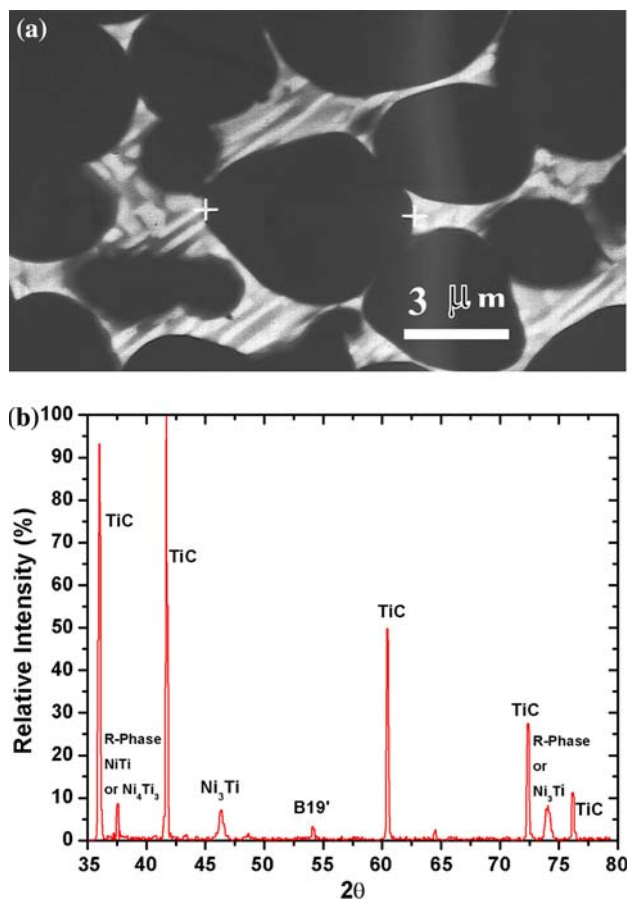
Fig. 8 (a) Backscattered electron micrograph of stoichiometric TiC–40NiTi. The microstructure, consisting of TiC particles surrounded by a two-phase matrix, is typical of composites synthesized with the anticipation of stoichiometric carbide formation. (b) X-ray diffraction scan for stoichiometric TiC–30NiTi
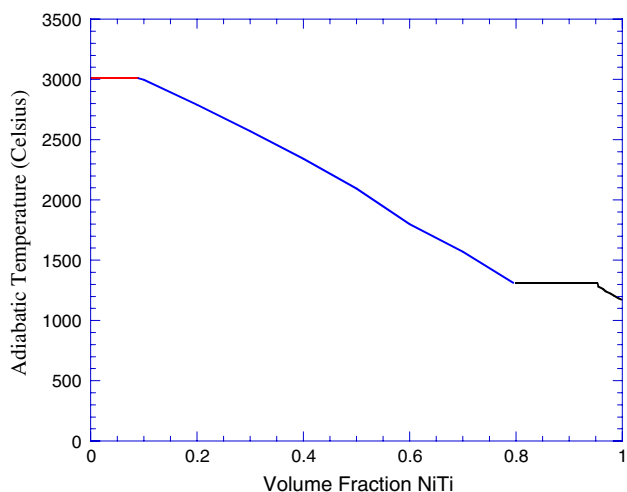


Fig. 9 Adiabatic temperature in TiC–NiTi system as a function of volume fraction of NiTi

function of its carbon-to-titanium ratio [22]. At a NiTi content of 50 wt%, Poletika et al. [30] determined that the stoichiometry of the carbide was $TiC_{0.7}$.

The stoichiometry of the carbide in the current work can be estimated by measuring peak positions in the XRD. Changes in the Ti/C atom ratio change the lattice parameter of the carbide [22]. These changes shift the $2\theta$ position of peaks in the XRD scan according to the formula $a^2 = \frac{\lambda^2 s}{4 \sin^2 \theta}$ where $a$ is the lattice parameter, $\lambda$ is the wavelength of the CuK$\alpha$ radiation (1.5406 Å), and $s = h^2 + k^2 + l^2$ ($h$, $k$, $l$ are the Miller indices of the scattering planes). Structure factor calculations for $TiC_x$ reveal that the allowed reflections only include combinations of $h$, $k$, $l$ that are either all even or all odd. Even though the Bragg condition is satisfied for mixed $h$, $k$, $l$, there are no diffraction peaks. The relative positions of atoms within the unit cell cause destructive interference. Since the systematic error in the lattice parameter decreases as $\theta$ increases [32], the highest angle peak was used to determine $a$. The highest angle $TiC_x$ measured in this research was at $2\theta = 76.2°$. Comparison with data from the JCPDS file shows that this peak results from scattering from the (222) plane, so $s = 12$ was substituted into the above equation.

Precise measurements of lattice parameter by XRD require careful machine calibration. In this research, the XRD machine was not calibrated to a standard. However, since $Ni_3Ti$ is a line compound it can be used to calibrate peak positions. The measured $2\theta$ peak positions of the $Ni_3Ti$ in the composites can be subtracted from the peak positions reported in the JCPDS file. This difference, $\Delta$, can then be added to the $TiC_x$ peak positions. Again, since the systematic error decreases as $\theta$ increases, only samples with a detectable $Ni_3Ti$ (220) peak were considered. Table 4 shows the measured $TiC_x$ position, the shift $\Delta$, the corrected $TiC_x$ peak position, the calculated lattice parameter, and the corresponding $TiC_x$ stoichiometry determined from Storms [22]. The average $TiC_x$ stoichiometry was $x = 0.6$.
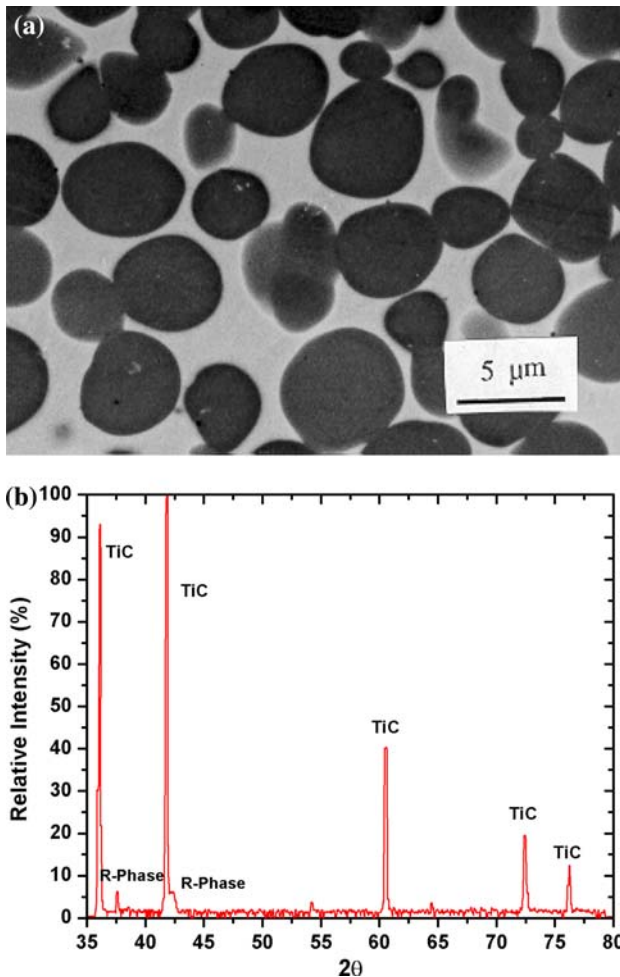
### $TiC_{0.7}$–NiTi composites

Figure 10a shows the backscattered electron micrograph of the $TiC_{0.7}$–40NiTi composite. The matrix appears to be composed of a single phase. Figure 10b shows the X-ray diffraction scan for $TiC_{0.7}$–30NiTi. All peaks corresponding to $Ni_3Ti$ have disappeared.

The XRD scans for larger samples (76 mm diameter, 300 g) mixed anticipating a carbide stoichiometry of 0.7 are shown in Fig. 11a–d. The $Ni_3Ti$ phase has been successfully suppressed. The matrix in the 20NiTi, 40NiTi, and 60NiTi composites is a combination of the $R$ and B19′ structures of NiTi. The 80 NiTi sample has only the $R$-phase structure. The peak positions for the $R$-phase were identified by comparison with those reported by Riva et al. [33].

**Table 4** Determination of $TiC_x$ stoichiometry from XRD peak positions

| Sample | Measured $TiC_x$ peak ($2\theta$) | Calibration shift $\Delta$ ($2\theta$) | Corrected $TiC_x$ peak ($2\theta$) | Lattice parameter (Å) | $TiC_x$ stoichiometry $x$ |
|---|---|---|---|---|---|
| TiC–30NiTi | 76.198 | 0.210 | 76.408 | 4.314 | 0.61 |
| TiC–40NiTi | 76.217 | 0.115 | 76.332 | 4.318 | 0.63 |
| TiC–50NiTi | 76.243 | 0.350 | 76.593 | 4.306 | 0.55 |



**Fig. 10** (**a**) Backscattered electron micrograph of nonstoichiometric $TiC_{0.7}$–40NiTi. The microstructure, consisting of spherical TiC particles surrounded by a NiTi matrix, is typical of composites synthesized with the anticipation of the formation of nonstoichiometric carbide. (**b**) X-ray diffraction scan for nonstoichiometric $TiC_{0.7}$–30NiTi

### $TiC_x$ particle size and morphology

Figure 12 shows the morphology of the ceramic reinforcement, which typically formed spheres with some particle faceting. Table 5 shows the $TiC_{0.7}$ particle size for various volume fractions of NiTi (30 mm diameter samples). The $TiC_{0.7}$ particle size decreased with increasing volume fraction of NiTi. The decrease in particle size with increasing volume fraction of NiTi was also observed in the 76 mm samples. However, the actual particle sizes, for a given volume fraction of NiTi, were larger for the 76-mm diameter compacts than in the 30 mm compacts because of slower cooling rates.

In the $TiC_{0.7}$–80NiTi composites, there were pockets of NiTi within the carbide particles. Dark field images revealed that the orientation of the NiTi entrapped within the carbide particles was the same as the surrounding matrix. Figure 13 shows a higher magnification image of the NiTi pockets.

Figure 14 shows the interface between the $TiC_{0.7}$ particles and the NiTi matrix. There was no visible contamination. This has an important bearing on mechanical properties, since interface decohesion is an important failure interaction mechanism, In contrast, the cermets made by Dunand and coworkers [2–5] had contamination in the interfaces.

### Mechanical properties

Since interest in $TiC_{0.7}$–NiTi composites was driven by its potential use as an armor material, a number of mechanical tests were performed. The Vickers hardness of the composites was measured using a Leco Microhardness Testing Machine model M-400-H1. The load was 1000 g for 15 s. The monolithic $TiC_{0.7}$ composition has a hardness below that of TiC [7, 34]. The hardness values of the $TiC_{0.7}$–NiTi composites, shown in Fig. 15, decrease with increasing volume fraction NiTi. The values fall between the predictions for the Voigt and Reuss averages. The fact that the hardness values fall below the linear (Voigt) interpolation is evidence that the plastic deformation is preferentially concentrated in the NiTi continuous matrix.

Focus was placed on the $TiC_{0.7}$–30NiTi composite, because it contains a large volume fraction of ceramic particles. Table 6 shows the transformation temperatures that were measured by acquiring calorimetry spectra between 20 and 150 °C. The following temperatures are given: on cooling, $R_{start}$ ($R_s$); $R_{finish}$ ($R_f$); on heating, Austenite$_{start}$ ($A_s$); Austenite$_{finish}$ ($A_f$). The net enthalpy of transformation was determined by calculating the area between the peak of the DSC curve and an estimated baseline. Although there was only one peak upon cooling, the net energy of transformation was greater than the total energy that would have been released if the entire matrix

**Fig. 11** X-ray diffraction scans for TiC$_{0.7}$–NiTi samples with initial compact size of 7.5 cm in diameter and 300 g. (**a**) TiC$_{0.7}$–20NiTi, (**b**) TiC$_{0.7}$–40NiTi, (**c**) TiC$_{0.7}$–60NiTi, and (**d**) TiC–80NiTi
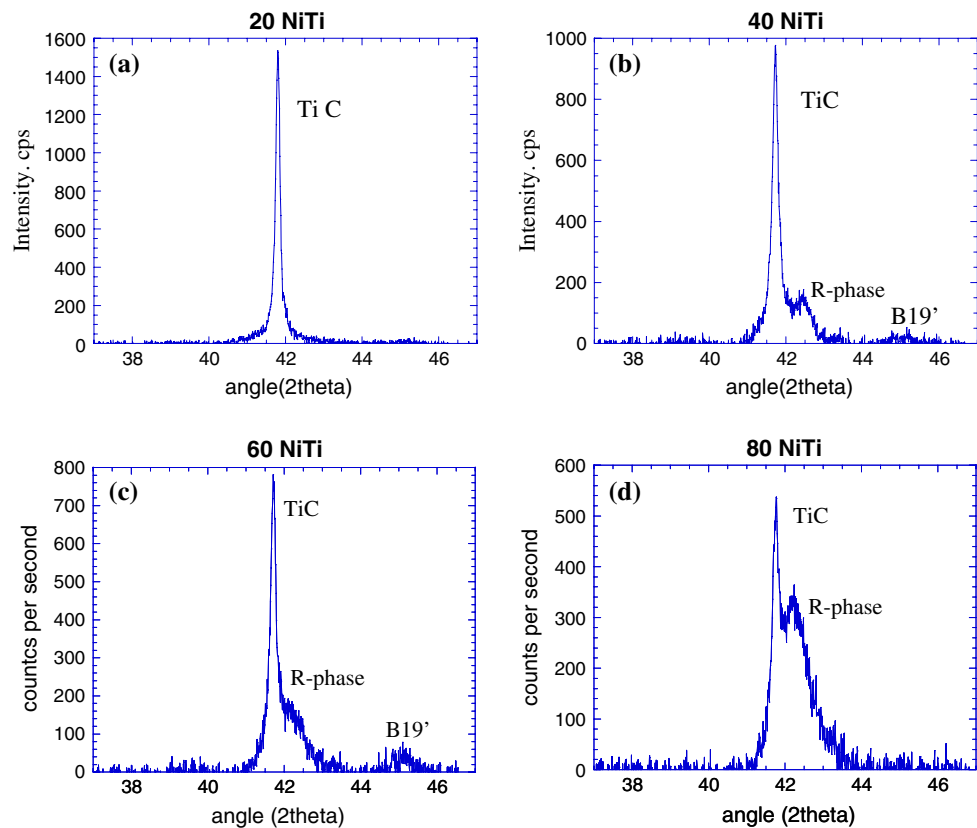


were to have transformed from B2 to $R$. Since Mari and Dunand [2] have shown that the stored elastic energy, the energy stored in defects, and the frictional work all reduce the observed exothermic reaction, those terms cannot account for the extra heat released. The extra energy can only be attributed to the formation of B19′. From the net enthalpy of transformation, the minimum amount of B19′ that must have formed was 18%. The remaining matrix was assumed to be $R$-phase.

Tests were conducted at temperatures below $R_f$, slightly above $R_s$, and above $A_f$. Both the loading and unloading response of the material were monitored.

Figure 16a shows the stress–strain curve of the TiC$_{0.7}$–30NiTi sample tested at room temperature. Upon unloading, the strain did not return to zero, during the first thermal cycle, as would be expected if the sample behaved completely elastically within this pressure range. During the second compression cycle on the same sample, the strain returned to zero upon unloading. The hypothesis that the irreversible strains are caused by an extraneous reason (like strain gage effect) cannot be discarded. However, it is strong evidence for reversible martensitic transformation. The companion paper [35] presents a comprehensive analysis on this.

Several quasi-static tests were also performed at higher temperatures. The same 30NiTi sample that was tested in

Fig. 16a was heated to $T_d = A_f + 20\ °C$ and then loaded to a maximum pressure of 2608 MPa and strain of 0.93%. Figure 16b shows the results. The stress–strain curve remains linear until approximately 0.8% strain. Then, there is an apparent bend in the curve. The yield point is at the maximum stress (2350 MPa) obtained in Fig. 16a. (Unfortunately, it is still not clear if this strain is from the adhesive or from the formation of stress-induced martensite. However, it is quite likely to be from the adhesive, because any B19′ that might have formed as a result of compressive loading at room temperature would be strain stabilized [4]. It would not be expected to revert to B2 upon heating to $T_d = A_f + 20\ °C$. Therefore, only those regions of $R$-phase that did not transform to B19′ previously could revert to B2 during heating and contribute to the observed yield behavior. Since the temperature is now above $A_f$, the measured yield point should be at a stress higher than the maximum stress reached in the previous test, not at the same stress.)

The elastic modulus of the 30NiTi sample, as determined from the slope of the stress–strain curve in Fig. 16a, is $E_{load} = 300$ GPa. The predicted modulus, calculated by the rule of mixtures, is 329 GPa for a 30NiTi composite with a B2 matrix and 315 GPa for a composite with a B19′ matrix. The compressive strength, measured by testing a sample to failure at room temperature, is 2.8 GPa. The strain to failure was 0.96%.

**Fig. 12** The particle morphology of the 7.6-cm diameter TiC$_{0.7}$–NiTi samples
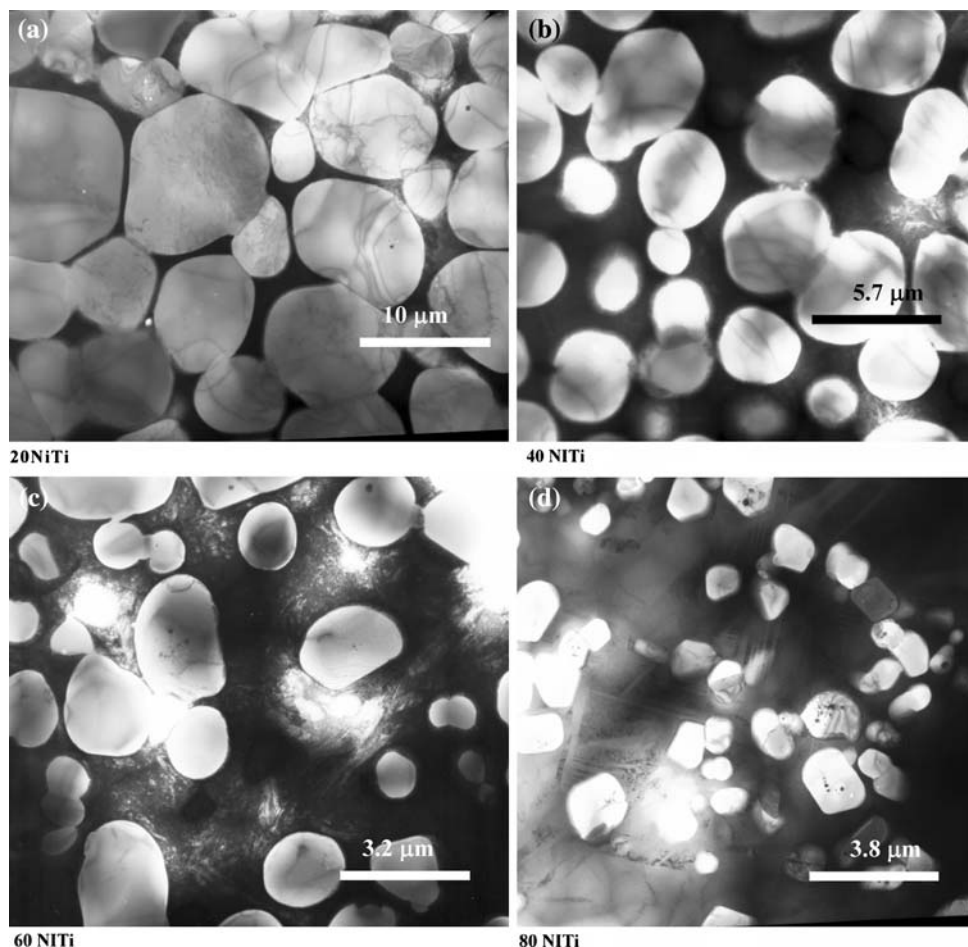


**Table 5** TiC$_x$ particle size as a function of NiTi content in TiC$_{0.7}$–NiTi composites (compact size 3 cm diameter, 25 g)

| Vol% NiTi | Average TiC$_x$ particle size (μm) | Average standard deviation (μm) |
|---|---|---|
| 30 | 6.9 | 1.8 |
| 40 | 3.9 | 1.0 |
| 50 | 2.7 | 0.7 |

Figure 17 shows the stress–strain curves for a 30NiTi specimen tested dynamically in the split Hopkinson bar at an average strain rate of $10^2$/s. In this case, the strains and stresses were measured by strain gages on the incident and transmission bars. The actual specimen was not instrumented with a strain gage. Since the sample did not fail, both the loading and unloading behavior were recorded. However, for more accurate measurements, strain gages should be directly attached to the test specimen.

In both quasi-static and dynamic tests where the 30NiTi specimens failed, fracture was by axial splitting. Figure 18 shows the fracture surface, in which there is very little evidence of ductile behavior in the NiTi. It appears to be essentially brittle fracture in which the TiC$_x$ particles have
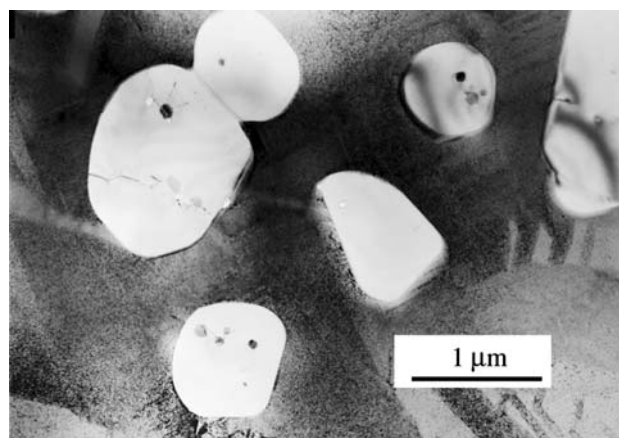


**Fig. 13** TEM image of TiC$_{0.7}$–80NiTi composite. The particles are faceted and contain pockets of entrapped NiTi

cleaved transgranularly. It is important to note that there is no evidence of preferential failure along the interface between the TiC$_{0.7}$ inclusions and the NiTi matrix. This supports the hypothesis that the TiC$_{0.7}$ particles are well bonded to the NiTi matrix and that the interface between the two phases is strong.
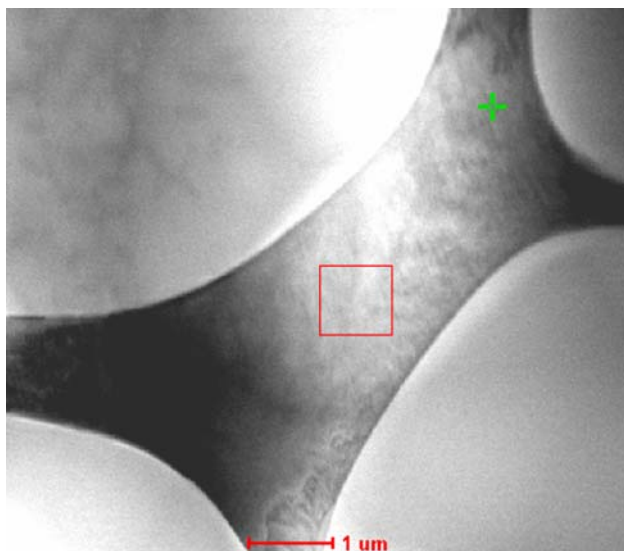
**Fig. 14** TEM of $TiC_{0.7}$–20vol%NiTi that shows the interface between the TiC particles and the NiTi matrix
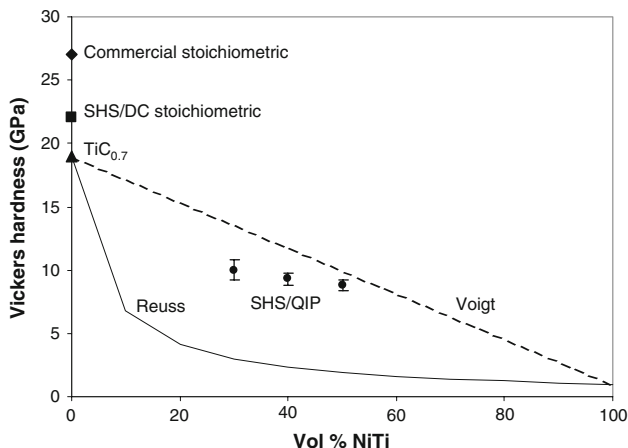


**Fig. 15** Vickers hardness of SHS/QIP $TiC_{0.7}$–NiTi composites compared to the hardness of monolithic TiC and $TiC_{0.7}$ (LaSalvia et al. [7] and Kosolapova [34])

| Table 6 Transformation temperatures in $TiC_{0.7}$–30NiTi measured by acquiring calorimetry spectra between 20 and 150 °C | | $TiC_{0.7}$–30NiTi (°C) |
| --- | --- | --- |
| | $R_s$ | 58 |
| | $R_f$ | 47 |
| | $T_s$ | 63 |
| | $A_s$ | 73 |
| | $A_f$ | 90 |

Flexural strength was measured using the four-point bending technique. The results are listed in Table 7. The samples for the bend tests were taken from a different plate than that used for the quasi-static compression tests. Some of the bend test samples had surface flaws and pores. Those specimens with surface flaws failed at much lower loads
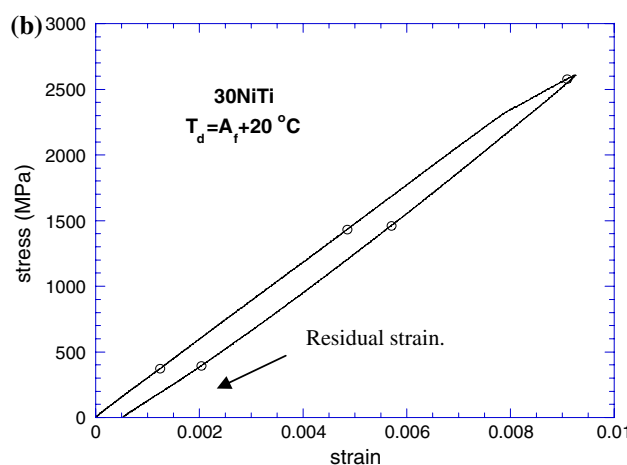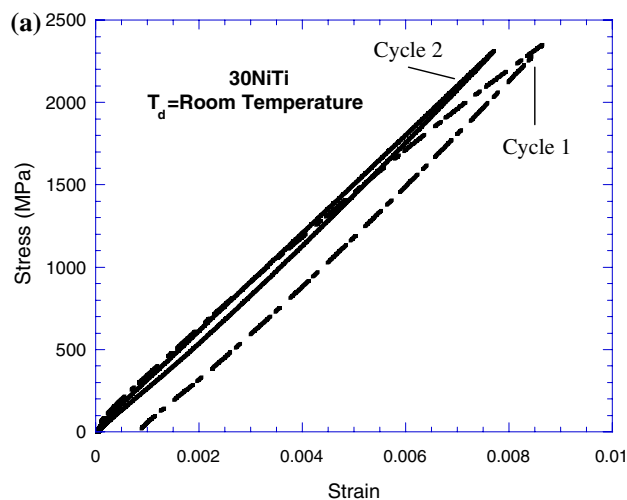


**Fig. 16** (**a**) Stress–strain curve for the $TiC_{0.7}$–30NiTi composite tested at a temperature room temperature and loaded to approximately 2350 MPa. (**b**) Stress–strain curve for $TiC_{0.7}$–30NiTi sample tested at $T_d = A_f + 20$ °C and loaded to 2600 MPa
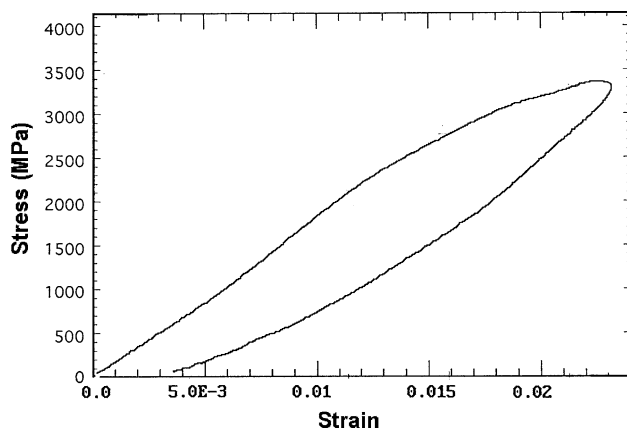


**Fig. 17** Stress–strain curve for $TiC_{0.7}$–30NiTi tested dynamically at a strain rate of $10^2$/s

than those specimens with no apparent defects. The average flexural strength for specimens with no visible flaws is 1047 MPa with a standard deviation of 90 MPa.
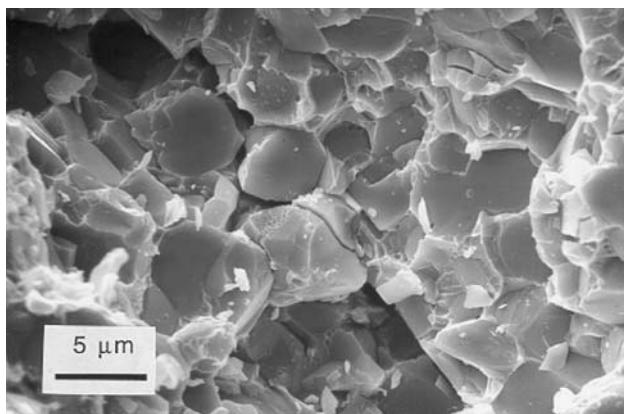
**Fig. 18** Fracture surface of failed $TiC_{0.7}$–30NiTi cermet

**Table 7** Flexural strength of $TiC_{0.7}$–30NiTi

| Sample number | Presence of visible surface flaws | Flexural strength (MPa) |
|---|---|---|
| 1 | Yes | 204 |
| 2 | No | 1095 |
| 3 | No | 1102 |
| 4 | Yes | 288 |
| 5 | Yes | 715 |
| 6 | No | 943 |

## Conclusion

TiC–NiTi composites were successfully synthesized by a technique combining self-propagating high-temperature synthesis (SHS) of elemental powders with densification by quasi-isostatic pressing (QIP). Composites with varying volume fractions of NiTi were produced, and the resulting structures and transformation behavior were characterized. The densification response of the reaction products was established and compared with predictions from the Fischmeister–Arzt and Torre–Carroll–Holt constitutive equations for porous materials. This comparison enabled the establishment of the flow stress, $\sigma_0$, of the product: varying between 10 and 30 MPa.

Powder mixtures prepared anticipating the formation of stoichiometric TiC result in the formation of composites with a eutectic matrix of $Ni_3Ti$ and NiTi. This titanium impoverishment of the matrix is consistent with the formation of nonstoichiometric $TiC_x$ during the combustion reaction. The $Ni_3Ti$ phase can be suppressed by anticipating the formation of $TiC_{0.7}$ and adjusting the chemical content of the reactant mixture to include additional titanium.

## References

1. Goldstein D (1977) US Patent 4,030,427
2. Mari D, Dunand DC (1995) Metall Mater Trans A 26A:2833. doi:10.1007/BF02669642
3. Dunand DC, Mari D, Bourke MAM, Roberts JA (1996) Metall Mater Trans A 27A:2820. doi:10.1007/BF02652374
4. Fukami-Ushiro KL, Dunand DC (1996) Metall Mater Trans A 27A:183. doi:10.1007/BF02647758
5. Fukami-Ushiro KL, Dunand DC (1996) Metall Mater Trans A 27A:193. doi:10.1007/BF02647759
6. Hoke DA, Meyers MA, Meyer LW, Gray GT III (1992) Metall Trans A 23A:77
7. LaSalvia JC, Meyer LW, Meyers MA (1992) J Am Ceram Soc 75:592. doi:10.1111/j.1151-2916.1992.tb07848.x
8. Olevsky E, Kristofetz E, Uzoigwe C, Meyers M (1997) Advances in Powder Metallugy and Particulate Materials, MPIF, 3-43
9. Olevsky EA, Kristofetz ER, Meyers MA (1998) Int J Comb Synth 7:517
10. Merzhanov AG, Borovinskaya IP (1972) Dokl Akad Nauk SSSR 204:366
11. Anselmi-Tamburini U, Munir ZA (1989) J Appl Phys 66:5039
12. Yi HC, Moore JJ (1990) J Mater Sci 25:1159. doi:10.1007/BF00585421
13. LaSalvia JC, Meyers MA (1995) Int J SHS 4:43
14. LaSalvia JC, Meyers MA, Kim DK (1994) J Mater Synth Process 2:255
15. LaSalvia JC, Kim DK, Meyers MA (1996) Mater Sci Eng A 206:71. doi:10.1016/0921-5093(95)09994-8
16. Hoke DA, Meyers MA (1994) J Am Ceram Soc 78:275. doi:10.1111/j.1151-2916.1995.tb08797.x
17. Skorohod V, Olevsky E, Shtern M (1993) Powder Metall Met Ceram N1(361):22
18. Skorohod V, Olevsky E, Shtern M (1993) Powder Metall Met Ceram N2(362):16
19. Olevsky E, Dudek HJ, Kaysser WA (1996) Acta Metall Mater 44:707
20. Olevsky EA, Strutt ER, Meyers MA (1998) Advances in Powder Metallurgy and Particulate Materials, MPIF, 3-93
21. Olevsky EA, Strutt ER, Meyers MA (2001) Scr Mater 44:1139. doi:10.1016/S1359-6462(01)00661-3
22. Storms EK (1967) The refractory carbides. Academic Press, Inc., New York and London
23. Merzhanov AG, Khaikin BI (1988) Prog Energy Combust Sci 14(1):98. doi:10.1016/0360-1285(88)90006-8
24. Raman RV, Rele SV, Poland S, LaSalvia JC, Meyers MA, Niiler AR (1995) JOM 47:23
25. Fischmeister HF, Arzt E (1983) Powder Metall 26:82
26. Helle AS, Easterling KE, Ashby MF (1985) Acta Metall 33:2163. doi:10.1016/0001-6160(85)90177-4
27. Torre C (1948) Berg-Huttenmann Monatsh Montan Hochschule Leoben 93:62
28. Carroll MM, Holt AC (1972) J Appl Phys 43:1626. doi:10.1063/1.1661372
29. Massalski TB (1990) Binary alloy phase diagrams. ASM International, Materials Park, Ohio

30. Poletika TM, Kul'kov SN, Panin VE (1983) Porosh Metall 7(247):54
31. Kul'kov SN, Poletiks TM, Chukhlomin AY, Panin VE (1984) Porosh Metall 8(260):88
32. Cullity BD (1978) Elements of x-ray diffraction. Addison-Wesley Publishing Company, Philippines
33. Riva G, Vanelli M, Airoldi G (1995) Phys Status Solidi A Appl Res 148:363. doi:10.1002/pssa.2211480204
34. Kosolapova TY (1990) Handbook of high temperature compounds: properties, production, applications. Hemisphere Publishing Corporation, New York
35. Paper 2: Combustion synthesis/quasi-isostatic pressing of $TiC_{0.7}$-NiTi cermets: microstructure and transformation characteristics